NASA/TM-2019-220273

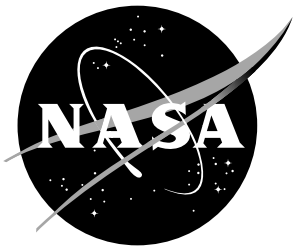

Numerical Study of the Effect of Mean Three-Dimensionality on Turbulence in Adverse-Pressure-Gradient Boundary Layers

G. N. Coleman and C. L. Rumsey
Langley Research Center, Hampton, Virginia

P. R. Spalart
Boeing Commercial Airplanes, Seattle, Washington

April 2019

NASA STI Program. . . in Profile

Since its founding, NASA has been dedicated to the advancement of aeronautics and space science. The NASA scientific and technical information (STI) program plays a key part in helping NASA maintain this important role.

The NASA STI Program operates under the auspices of the Agency Chief Information Officer. It collects, organizes, provides for archiving, and disseminates NASA's STI. The NASA STI Program provides access to the NASA Aeronautics and Space Database and its public interface, the NASA Technical Report Server, thus providing one of the largest collection of aeronautical and space science STI in the world. Results are published in both non-NASA channels and by NASA in the NASA STI Report Series, which includes the following report types:

- TECHNICAL PUBLICATION. Reports of completed research or a major significant phase of research that present the results of NASA programs and include extensive data or theoretical analysis. Includes compilations of significant scientific and technical data and information deemed to be of continuing reference value. NASA counterpart of peer-reviewed formal professional papers, but having less stringent limitations on manuscript length and extent of graphic presentations.
- TECHNICAL MEMORANDUM. Scientific and technical findings that are preliminary or of specialized interest, e.g., quick release reports, working papers, and bibliographies that contain minimal annotation. Does not contain extensive analysis.
- CONTRACTOR REPORT. Scientific and technical findings by NASA-sponsored contractors and grantees.
- CONFERENCE PUBLICATION. Collected papers from scientific and technical conferences, symposia, seminars, or other meetings sponsored or co-sponsored by NASA.
- SPECIAL PUBLICATION. Scientific, technical, or historical information from NASA programs, projects, and missions, often concerned with subjects having substantial public interest.
- TECHNICAL TRANSLATION. English-language translations of foreign scientific and technical material pertinent to NASA's mission.

Specialized services also include organizing and publishing research results, distributing specialized research announcements and feeds, providing information desk and personal search support, and enabling data exchange services.

For more information about the NASA STI Program, see the following:

- Access the NASA STI program home page at `http://www.sti.nasa.gov`
- E-mail your question to `help@sti.nasa.gov`
- Phone the NASA STI Information Desk at 757-864-9658
- Write to:
  NASA STI Information Desk
  Mail Stop 148
  NASA Langley Research Center
  Hampton, VA 23681-2199

NASA/TM-2019-220273

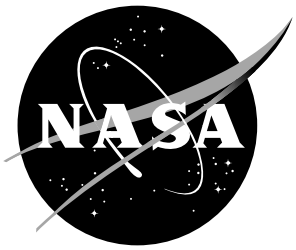

Numerical Study of the Effect of Mean Three-Dimensionality on Turbulence in Adverse-Pressure-Gradient Boundary Layers

G. N. Coleman and C. L. Rumsey
Langley Research Center, Hampton, Virginia

P. R. Spalart
Boeing Commercial Airplanes, Seattle, Washington

National Aeronautics and
Space Administration

Langley Research Center
Hampton, Virginia 23681-2199

April 2019

Acknowledgments

This research was sponsored by the NASA Transformational Tools and Technologies (TTT) Project of the Transformative Aeronautics Concepts Program under the Aeronautics Research Mission Directorate. Computations were performed on resources provided by the NASA Advanced Supercomputing (NAS) Division. Dr M. Strelets made useful comments.

Available from:

NASA STI Program / Mail Stop 148
NASA Langley Research Center
Hampton, VA 23681-2199
Fax: 757-864-6500

Abstract

Direct numerical simulation (DNS) is used to isolate the influence of sweep on a separating turbulent boundary layer. Attention here is limited to the behavior of the turbulence within the adverse-pressure-gradient (APG) region upstream of separation. Other regions and quantities are considered in Coleman, Rumsey & Spalart [1]. The mean three-dimensionality and outer-layer inviscid skewing have only a slight effect upon the structure of the turbulence (measured by the relationship of the components of the Reynolds-stress tensor and the efficiency of the turbulence energy transfer) compared with that of the adverse pressure gradient, which dominates both the skewed and unskewed layers.

1 Introduction

This note examines the manner in which turbulent boundary layers are affected by sweep – that is, by misalignment between the pressure gradient and the freestream velocity vector. The resulting three-dimensional boundary layer (3DBL) is characterized by mean velocities and vorticities that change direction as well as magnitude with distance from the surface. We consider the spatially developing incompressible turbulent 3DBL over an idealized – flat, smooth – 35-degree infinite swept wing that develops by applying a prolonged adverse then favorable pressure gradient (APG and FPG, respectively) in the 'chordwise' direction (normal to the leading edge) to an originally two-dimensional (2D) mean state with nonzero spanwise (parallel to the leading edge) mean velocity. Note that this use of 'spanwise' and 'chordwise' is not uniform aeronautical terminology, since these sometimes indicate directions, respectively, normal and parallel to the direction of flight (cf. Bradshaw & Pontikos [2]); the direction of flight itself will be referred to here as 'streamwise'. Following Driver & Johnston [3], we shall describe as 'collateral' any 2D boundary layer – such as the initial 2D state just mentioned – whose nonzero spanwise component of mean velocity is solely an artifact of the orientation of the coordinate system.

Direct numerical simulation (DNS) is used to create a computational version of the infinite-swept-wing experiments of Bradshaw & Pontikos [2] and especially, since it also involves separation, of van den Berg *et al.* [4]. This effort continues and generalizes our work on unswept turbulent separation bubbles, presented in Coleman, Rumsey & Spalart [5] (henceforth denoted CRS18), and supplements the broader study of swept separation in Coleman *et al.* [1] (henceforth CRS19). The latter contains a discussion of the validity of the swept-wing Independence Principle for the turbulent case, and implications for Reynolds-averaged turbulence models. Here we focus solely on the role of mean three-dimensionality in the evolution of the energetics and structure of the turbulence in APG boundary layers leading up to separation.

Table 1. Case parameters.[1]

Case	σ (deg.)	$U_\infty Y/\nu$	$U_\infty\theta_{x_0}/\nu$	$Q_\infty\theta_{x_0}/\nu$	$V_{\max}/U_\infty$	ς/Y	$\varphi_{\rm top}/U_\infty$
C0	0	80 000	3057	3057	0.1333	3.66	0.0034
C35	35	80 000	3031	3700	0.1333	3.66	0.0038

[1]Sweep angle $\sigma = \arctan(W_\infty/U_\infty)$. Chordwise component of upstream/reference velocity magnitude is U_∞, such that the total/streamwise magnitude is $Q_\infty = U_\infty/\cos\sigma = (U_\infty^2 + W_\infty^2)^{1/2}$, where W_∞ is the spanwise component.

2 Approach and flow definition

The equation set and numerical strategy are identical to those used in CRS18, to which the reader is referred for details. The approach involves pseudospectral DNS of a fully turbulent incompressible ZPG boundary layer over a flat no-slip surface, subjected to first APG then FPG conditions (figure 1). The chordwise (x-direction) pressure gradients are induced by a transpiration profile $V_{\rm top}(x)$ through a parallel plane offset a fixed distance Y from the no-slip surface. The strength and duration of the pressure gradients are set by the maximum velocity $V_{\max}$ and length-scale ς of the transpiration profile,

$$V_{\rm top}(x) = -\sqrt{2}V_{\max}\left[\frac{x}{\varsigma}\right]\exp\ \left(\frac{1}{2} - \left[\frac{x}{\varsigma}\right]^2\right) + \varphi_{\rm top}, \qquad (1)$$

with $x = 0$ defined as the location at which $V_{\rm top}$ changes from suction to blowing (see figure 2a). The last term in (1), $\varphi_{\rm top}$, is the magnitude of a (small) constant 'bleed' velocity, adjusted to offset the blockage in the nominally ZPG regions, and thereby produce $\mathrm{d}P/\mathrm{d}x \approx 0$ along the wall there.

The new boundary condition on the spanwise velocity is enforced by adding $(1-\exp(-y/y_0))W_\infty$, where y_0 is the Jacobi-to-physical-space mapping lengthscale and W_∞ the constant spanwise velocity above the layer, to the spanwise component of the computational variable $\mathbf{U_1}$ (see Spalart, Moser & Rogers [6] and Spalart & Coleman [7]). The mean vorticity and mean viscous terms are altered as in Coleman, Ferziger & Spalart [8]. The corresponding change to the finite-domain version (equivalent to the $y \to \infty$ form used here) of the top-wall boundary condition is the replacement of $\partial w/\partial y = 0$ with $w = W_\infty$ in (2.2c) of CRS18.

We consider a single new case, denoted C35, which is a $\sigma = 35°$ infinite-swept-wing version of Case C of CRS18, in the sense that the transpiration profile – and thus the pressure-gradient variation – of the latter is applied along the chordwise direction of the swept flow, with the same chordwise Reynolds number $U_\infty Y/\nu$. We shall henceforth refer to Case C, the highest-Reynolds-number flow presented in CRS18, as 'Case C0', as a reminder of its unswept state. As was true for Case C0, the combination of transpiration parameters shown in table 1 leads to an APG/FPG variation that creates a small separation 'bubble' (strip), with mean detachment/reattachment lines parallel to the leading edge. Figure 2 provides an overall comparison of Cases C0 and C35. They have identical $U_{\rm top}$ and $V_{\rm top}$, with

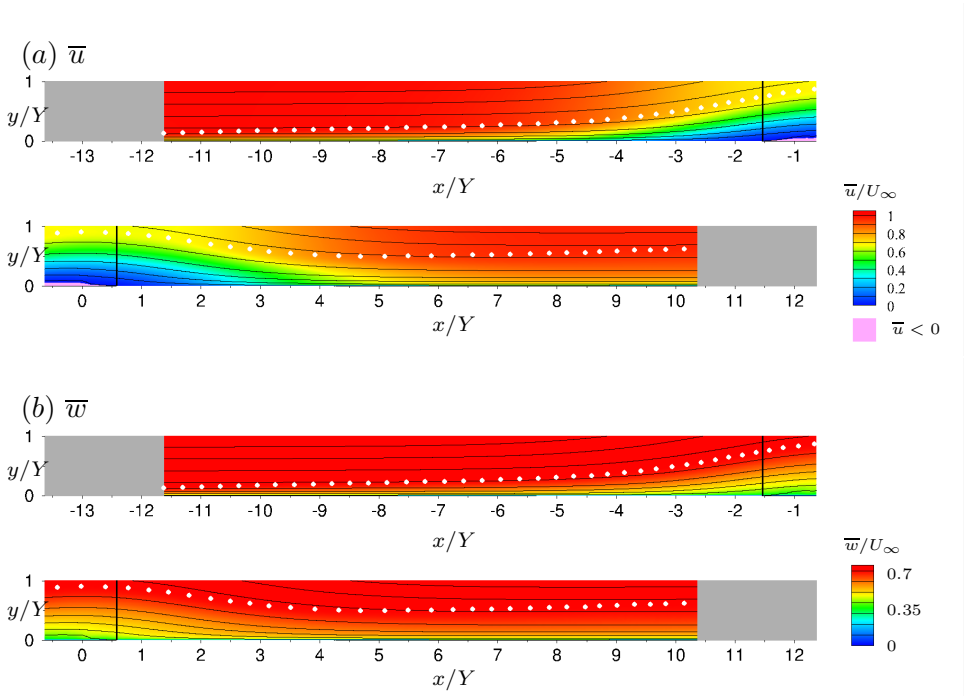

Figure 1. Mean streamlines and and contours of (a) chordwise $\overline{u}$ and (b) spanwise $\overline{w}$ velocity in chordwise–wall-normal plane for Case C35. Shaded/grey regions are fringe zones. Solid vertical lines indicate locations at which mean chordwise wall stress is zero. White symbols denote edge of boundary layer.

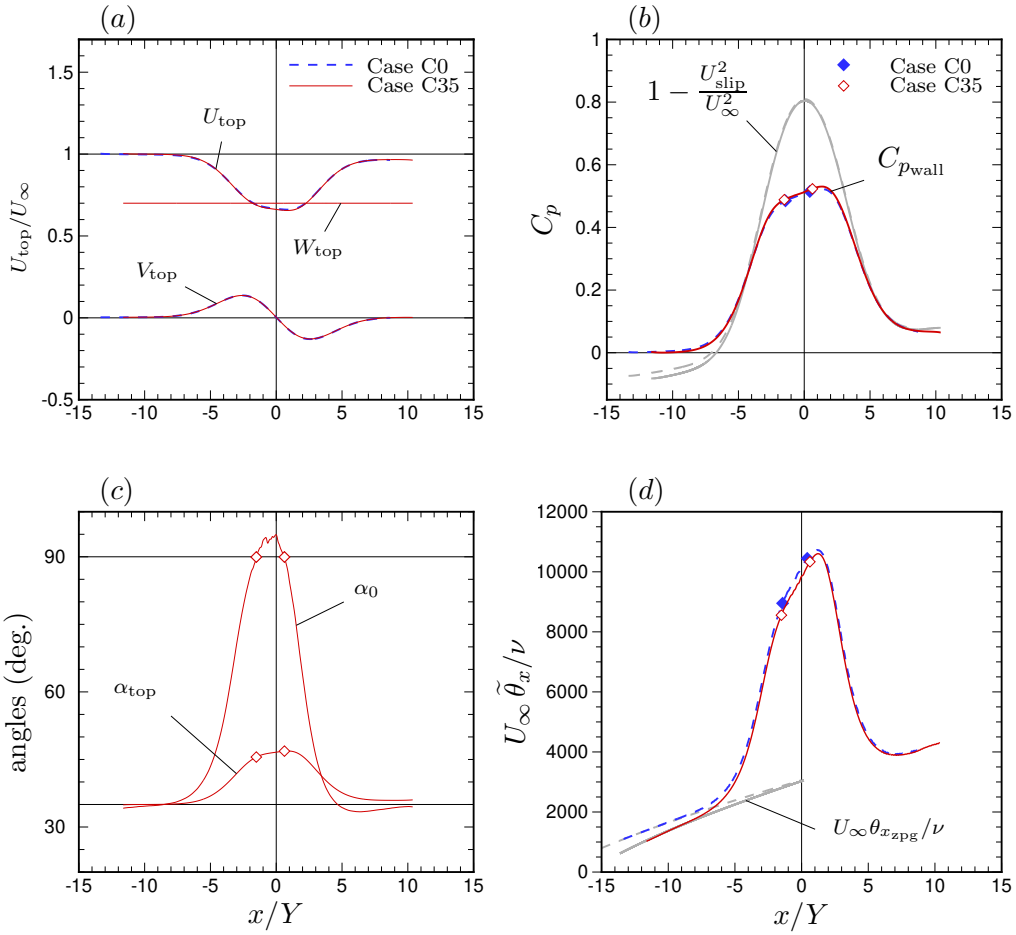

Figure 2. Chordwise variation of (a) velocity components at $y = Y$, (b) mean wall pressure, $C_{p_{\rm wall}} = (\overline{p}_{\rm wall} - P_\infty)/\frac{1}{2}\rho U^2_\infty$, ($c$) angles of surface-shear $\alpha_0 = \arctan(\tau_{w_z}/\tau_{w_x})$ and velocity at $y = Y$, $\alpha_{\rm top} = \arctan(W_{\rm top}/U_{\rm top})$, and ($d$) chordwise momentum-thickness Reynolds number: Symbols, $\tau_{w_x} = 0$ locations; shaded/grey curves, (in b) blockage-free wall-pressure variation associated with slip velocity $U_{\rm slip}$ induced by $V_{\rm top}$ (see CRS18), and (in d) virtual Reynolds-number variation given by ZPG thickness $\theta_{x_{\rm zpg}}$ from Coles [9] (see figure 3b and its legend). Chordwise momentum thickness $\widetilde{\theta}_x$ defined in terms of mean spanwise vorticity (equation (3.4) of CRS18).

finite W_{top} distinguishing C35 (figure 2*a*). Figure 2*b* shows the wall pressure (including the blockage-free variation). Figure 2*c* illustrates the change along the chordwise axis of the directions of the local wall shear and top-wall velocity for Case C35, and figure 2*d* presents the chordwise momentum-thickness Reynolds numbers.

In order to make the comparison between the swept and unswept flows as meaningful as possible (when, for example, examining the validity of the Independence Principle), Case C35 is defined such that the momentum-thickness Reynolds number of its mean chordwise velocity component in the ZPG region upstream of transpiration, and that of the mean streamwise component in the same region of Case C0, 'aim at the same target'. This is done by adjusting the $x = 0$ location of the Case C35 transpiration profile such that the chordwise ZPG layer's virtual thickness θ_{x_0} at $x = 0$ (defined as the thickness that would exist were the APG not applied) is close to the virtual $x = 0$ thickness of Case C0. The matching is based on the behavior observed in the Coles [9] experiments, using the $C_f = C_f(\mathrm{Re}_\theta)$ interpolant shown in figure 3*b*, and the ZPG von Karman momentum integral equation. The result is that $U_\infty \theta_{x_0}/\nu \approx 3000$ for both the $\sigma = 0$ and 35° cases (see table 1 and shaded/grey curves in figure 2*d*). At the ZPG reference stations (see below), the streamwise Reynolds number has increased from $Q_\infty \theta/\nu = 1744$ for Case C0 to 2052 for Case C35.

The Case C0 and C35 numerical parameters are summarized in table 2. The chordwise Λ_x and spanwise Λ_z domain sizes, and the number of wall-normal N_y and spanwise N_z quadrature points are the same. The chordwise resolution, Λ_x/N_x, was increased from $N_x = 7680$ to 15360 to accommodate the finer scales associated with the misalignment between x and the streamwise direction of the swept flow (illustrated in figure 4*b*, *c* of CRS19). The spatial resolution in wall units shown in table 2, which is based on the maximum total skin friction within the domain, near the beginning of the upstream ZPG layer, is comparable to that employed for Case C0, and thus broadly sufficient. (See CRS18 for a discussion of the somewhat-marginal spanwise resolution in the ZPG region, and a caveat regarding the wall-normal resolution above the edge of the boundary layer over the bubble.) The differences in the inflow and outflow coordinates, x_{in} and x_{out}, are the result of altering the $x = 0$ transpiration location as described above.

The chordwise (x) boundary conditions are applied using the 'fringe method' introduced by Spalart & Watmuff [10], which involves adding forcing terms to the governing equations that are only active in the inflow and outflow regions of the domain, indicated by the shaded/grey zones in figure 1. This allows the chordwise-periodic spectral discretization to accommodate the x-wise variation of the mean flow (cf. figure 1). The fringe parameters used here are identical to those specified in Appendix A of CRS18 (i.e., $x_1/Y = 1.0$, $V_2/U_\infty = 1.5$, $\Upsilon = 2.0$, $y_\beta/Y = 0.16$), except for y_α/Y, which was decreased from 0.518 to 0.455. The spectral algorithm imposes periodic boundary conditions in the spanwise infinite-sweep direction z, and employs Jacobi polynomials, mapped to the semi-infinite domain, in the wall-normal direction y (Spalart, Moser & Rogers [6]).

Statistics were gathered by averaging over z and in time, involving 78 full x-y fields over periods of 33.5 and $54Y/U_\infty$, respectively, for Cases C0 and C35, corresponding to 1.3 and 2.1 domain-flow-through times Λ_x/U_∞. Some quantities were

Table 2. Numerical parameters.[2]

Case	Λ_x/Y	$x_{\rm in}/Y$	$x_{\rm out}/Y$	Λ_z/Y	N_x	Δx^+	N_y	y^+_{10}	N_z	Δz^+
C0	26	−15.35	10.65	4.0	7680	12.3	240	4.6	2560	6.0
C35	26	−13.63	12.37	4.0	15 360	7.7	240	5.7	2560	7.1

[2]Origin of chordwise coordinate x, and thus locations of inflow $x_{\rm in}$ and outflow $x_{\rm out}$ stations, is defined by location of sign change of transpiration profile $V_{\rm top}(x)$, with $x_{\rm out} - x_{\rm in} = \Lambda_x$, where Λ_x is the streamwise period of the domain (see figure 2*a* and main text); spanwise period is Λ_z. Dealiasing is enforced by defining the number of quadrature/collocation points, N_x, N_y and N_z, such that they are related to the number of streamwise, wall-normal and spanwise Galerkin spectral expansion coefficients, respectively, by $M_x = 2N_x/3$, $M_y = (2N_y - 9)/3$ and $M_z = 2N_z/3$. Spatial resolution is quantified in terms of the quadrature grid, such that $\Delta x = \Lambda_x/N_x$ and $\Delta z = \Lambda_z/N_z$; the distance y_{10} is that of the tenth wall-normal quadrature point from the bottom of the domain (with $y_1 = 0$). Wall units, e.g., $\Delta x^+ = \Delta x\, u_\tau/\nu$ and $y^+_{10} = y_{10}\, u_\tau/\nu$, are based on maximum skin friction within the domain, downstream of the fringe zone.

also locally averaged in x, with a filter width as large as $0.1Y$. The momentum balances associated with the resulting statistics are very good, comparable, in both the x and z directions, to the x balance shown in Appendix C of CRS18.

Computations were run on the NASA Advanced Supercomputing (NAS) Division's Pleiades system, a distributed-memory SGI ICE cluster, on from 1024 to 4096 cores. A total of about 512 000 CPU-core-hours were utilised during the statistics-gatherings phase of the Case C35 computations.

3 ZPG reference state

A high priority for the design of this flow was to specify canonical ZPG conditions upstream of the APG. This is an essential feature for DNS (or experimental) data that is to be used to isolate PG effects and to serve as a benchmark for RANS-model testing, or that of other turbulence-resolving approaches for that matter. The extent to which this objective was met can be inferred from figure 3. The ZPG reference station was chosen as $x/Y = -9.5$ and -8.5, respectively, for Cases C0 and C35. The mean-velocity profiles, the displacement/momentum-thickness shape factor, and the skin friction are all characteristic of constant-freestream-velocity boundary layers at their respective Reynolds numbers ($\mathrm{Re}_\theta = 1744$ for C0, 2052 for C35; the corresponding friction velocities are $u_\tau/U_\infty = u_\tau/Q_\infty = 0.0436$ for C0, and $u_\tau/U_\infty = 0.0525$, $u_\tau/Q_\infty = 0.0430$ for C35). We note the logarithmic-law scaling of the mean velocity in figure 3*a*, in agreement between all DNS datasets and Luchini's proposed high-Reynolds-number asymptote, and that the Re_θ dependence of δ^*/θ and C_f (figure 3*b*) for both cases compares well with previous DNS [11]-[13], and the Coles [9] data for ZPG boundary layers. The Case C35 TKE profile and individual budget terms (not shown), also agree well with Schlatter & Örlü's (2010) ZPG DNS at $\mathrm{Re}_\theta = 2000$ (as it did for Case C0; see figure 6 of CRS18), although the

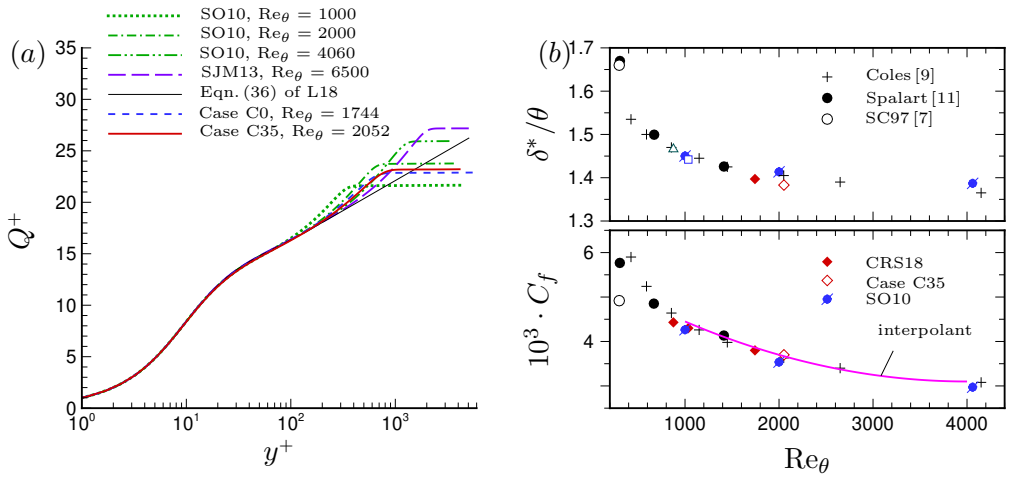

Figure 3. (a) Mean-velocity profiles at ZPG reference stations, and ZPG-TBL DNS of Schlatter & Örlü [12] (SO10) and Sillero, Jiménez & Moser [13] (SJM13): ——, equation (36) of Luchini [14] (L18). (b) Shape factor and skin friction: ——, interpolant of Coles data: $C_f = a + b\mathrm{Re}_\theta + c\mathrm{Re}_\theta{}^2$, with $(a, b, c) = (0.0055, -1.2 \times 10^{-6}, 1.5 \times 10^{-10})$, where $C_f = \tau_w / \frac{1}{2}\rho Q_\infty^2$.

correspondence for the Case C35 outer-layer TKE profile is not quite as good as it is for Case C0. This agreement, for various quantities, underlines the success of the fringe-zone inflow/outflow treatment, in allowing a spatially developing flow to be faithfully represented in a periodic domain, and the sufficient length of development toward a universal ZPG state defined solely by Re$_\theta$.

The solid line in figure 3b is a curve-fit of the C_f versus Re$_\theta$ relationship found in the Coles results. As mentioned above, this was used to estimate the chordwise variation of the chordwise momentum thickness of the virtual (chordwise) ZPG boundary layer into the APG region – and thus set the origin (i.e., location of the APG-to-FPG transition) for the transpiration profile $V_{\mathrm{top}}(x)$, so that θ_x at $x = 0$, θ_{x_0}, for Case C35 is close to $\theta_{x_0} = \theta_0$ for Case C0; see figure 2a, d.

4 Effect of sweep on TKE and its rate of production

We begin by examining the impact of the 35-degree sweep on the development of the turbulence kinetic energy (TKE), focusing on the APG-induced evolution downstream of the ZPG states in Cases C0 and C35. This evolution will clarify the role of the misalignment between the negative 2D-APG strain S_{11} and the ZPG freestream velocity for the swept flow – or equivalently, in terms of axes $\widehat{x}_i$ aligned with/orthogonal to the freestream velocity, the role of the nonzero mean skewing $\widehat{S}_{13}$ and lateral $\widehat{S}_{33}$ strain-rate components, and the weakened streamwise deceleration $\widehat{S}_{11}$, associated with S_{11}. (Recall that in terms of the freestream-aligned components, the chordwise deceleration S_{11} transforms to $\widehat{S}_{11} = S_{11}\cos^2\sigma$, $\widehat{S}_{33} = S_{11}\sin^2\sigma$ and $\widehat{S}_{13} = \widehat{S}_{31} = -S_{11}\sin\sigma\cos\sigma$.) The effect-of-sweep comparison is complicated

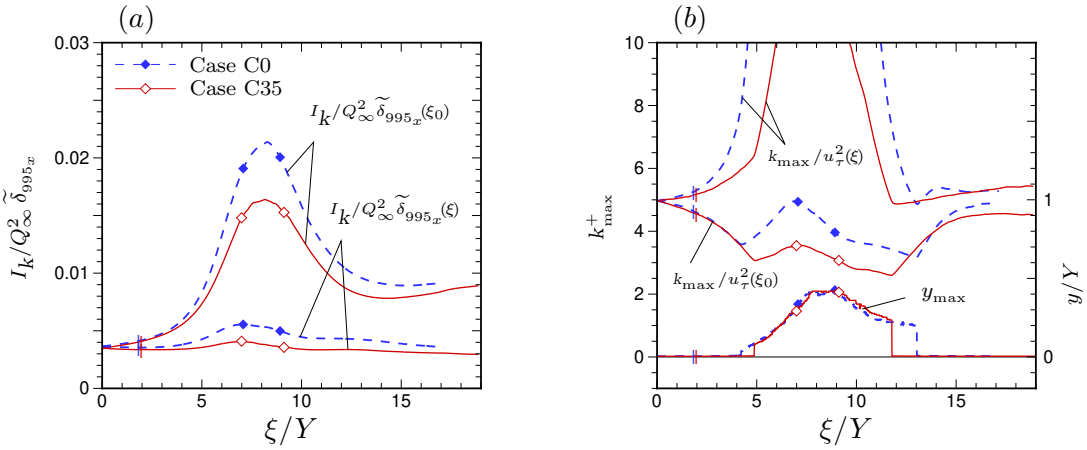

Figure 4. Chordwise variation of (*a*) integrated TKE $I_k = \int_0^Y k\,\mathrm{d}y$, and (*b*) maximum TKE (over y) $k_{\max}$ and its wall-normal location $y_{\max}$. The origin $\xi_0 = 0$ of the shifted chordwise coordinate $\xi = x - x_{\mathrm{ZPG35}}$ coincides with the Case C35 ZPG reference station $x_{\mathrm{ZPG35}} = -8.5Y$. Symbols mark locations at which mean chordwise wall shear stress $\tau_{w_x} = 0$. Small vertical lines near $\xi/Y = 2$ correspond to the chordwise station ($x/Y \approx -6.5$) at which $C_{p_{\mathrm{wall}}}$ rises to 0.10 of its maximum value (see figure 2*b*).

somewhat by the two ZPG states having different velocity-to-thickness ratios, such that at $x/Y = -8.5$[3], a given S_{11} strain is about 35% larger in units of $u_\tau/\widetilde{\delta}_{995_x}$ or $Q_\infty/\widetilde{\delta}_{995_x}$ for Case C0 than it is for Case C35. (See CRS19 for definition of the vorticity-based chordwise 99.5% boundary-layer thickness $\widetilde{\delta}_{995_x}$.) We will thus be especially interested in similarities between the two flows, since these will indicate behavior unaffected by sweep.

To emphasize the 2D-to-3D conversion effected by the APG, the chordwise axis ξ in figures 4 and 5 has been shifted such that its origin corresponds to the ZPG reference at $x/Y = -8.5$. The nominal beginning of the APG region has been defined as the station at which the mean wall pressure reaches 10% of its maximum value, above the separation bubble (figure 2*b*); this location is noted in figures 4 and 5 by the small vertical mark near $\xi/Y = 2$.

The growth of the integrated TKE across the layer, $I_d = \int_0^Y k\,\mathrm{d}y$, brought about by the APG is shown in figure 4*a*. The difference in the largest values, which for both flows occur above the bubble, correlates well with the difference in the strain-rate magnitude relative to the ZPG velocity-thickness ratios cited above, which is about 35% larger for Case C35. The smaller I_d values within the swept flow are roughly proportional to the local layer thickness, such that the 'energy density' $I_d/Q_\infty^2\widetilde{\delta}_{995_x}$ is fairly constant over each of the ZPG, APG and FPG regions (lower curves in figure 4*a*); this scaling also successfully accounts for the variation found in both flows immediately above the bubble. For both cases, the APG-induced growth

[3]The $x/Y = -8.5$ station is chosen here as the ZPG reference for both cases, despite $x/Y = -9.5$ defining the Case C0 ZPG state in CRS18, to provide the same 'initial conditions' for the APG straining history, in terms of the mean wall pressure variation. See below.

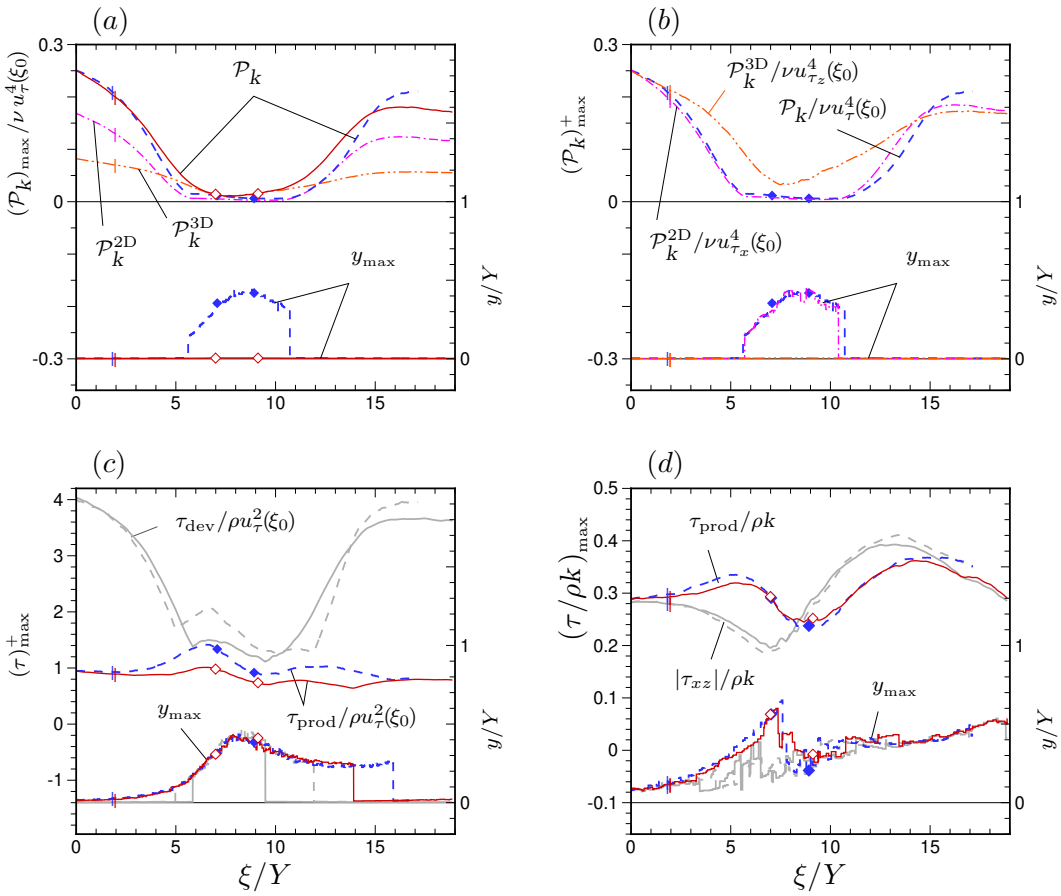

Figure 5. Chordwise variation of (a, b) y-maximum and location of TKE production rate $\mathcal{P}_k = -\overline{u_i' u_j'} S_{ij}$, (c) y-maximum and location of the productive shear stress $\tau_{\rm prod} \equiv \rho \mathcal{P}_k / \sqrt{2 S_{ij} S_{ij}}$ and the norm of Reynolds-stress deviator $\tau_{\rm dev} = \rho \sqrt{d_{ij} d_{ij}/2}$ where $d_{ij} = \overline{u_i' u_j'} - (2k/3)\delta_{ij}$, and (d) y-maximum and location of turbulence-to-mean energy transfer efficiency $\tau_{\rm prod}/\rho k$ and turbulence stress-energy ratio $|\tau_{xz}|/\rho k$, where the x, z-plane shear-stress magnitude $|\tau_{xz}| = \rho(\overline{u'v'}^2 + \overline{v'w'}^2)^{1/2}$: - - -, Case C0; ———, Case C35; —·— (in a, b), $\mathcal{P}_k^{\rm 2D} = -\overline{u_i' u_j'} S_{ij}$, $(i, j) \in (1, 2)$ (i.e., omitting terms involving spanwise direction $x_3 = z$) for Case C35; —··— (in a, b), $\mathcal{P}_k^{\rm 3D} = -2\overline{u'w'} S_{13} - 2\overline{v'w'} S_{23}$ for Case C35.

of the total TKE within the layer is accompanied by a reduction of the near-wall maximum $k_{\max}$ (figure 4*b*), associated with reduced mean skin friction C_f (figure 6*b* of CRS19). The maximum TKE in figure 4*b* is normalized by the total friction velocity u_τ, defined by both components of the wall shear stress, at either the ZPG reference station, $u_\tau(\xi_0)$, or at the local chordwise location, $u_\tau(\xi)$. The decreases of $k_{\max}$ in the ZPG-to-APG regions of Cases C0 and C35 are quite similar. The growth of $k_{\max}$ relative to the local wall stress $u_\tau^2(\xi)$ in the ZPG region, between $\xi = 0$ and 2, observed in figure 4*b*, is a symptom of increasing Reynolds number there; see figure 2*d* and Spalart [11]. While the sweep has little influence on the near-wall $k_{\max}$ reduction fairly far into the APG region, it does affect the chordwise location at which the outer-layer peak in the TKE profile becomes larger than the near-wall peak (cf. figure 12*a* of CRS18), with this location occurring sooner (smaller ξ) for the unswept case. The station downstream of the bubble at which $k_{\max}$ returns from the outer to the near-wall region, under the influence of the favorable- and zero-pressure gradients, also occurs at larger ξ for Case C0. That the $k_{\max}$ location for the swept flow remains near the wall longer within the APG, and begins again sooner within the FPG, is a consequence of the 'extra' TKE production contributed by the spanwise shear, which persists across the separation/reattachment zone (see below). The difference in magnitudes of the outer-layer $k_{\max}$ above the bubble again correlates with the difference in the magnitude of the APG/FPG strain $S_{11} = -S_{22}$ relative to the ZPG-boundary-layer parameters $u_\tau(\xi_0)$ and $\widetilde{\delta}_{995_x}(\xi_0)$.

The presence of sweep does not alter the similarity of the outer-layer trajectories of the $k_{\max}$ heights, $y_{\max}(\xi)$, or the fact that for both flows the maximum $k_{\max}$ – which for Case C0 is close to its upstream ZPG value – is found immediately above the mean separation.

A comparison of the maximum TKE production rate $\mathcal{P}_k$ is shown in figures 5(a, b); also included, for Case C35, are the separate contributions to $\mathcal{P}_k$ made by the chordwise ($\mathcal{P}_k^{2\mathrm{D}}$) and spanwise ($\mathcal{P}_k^{3\mathrm{D}}$) terms, where $\mathcal{P}_k^{2\mathrm{D}} = -\overline{u'u'}S_{11} - 2\overline{u'v'}S_{12} - \overline{v'v'}S_{22}$ and $\mathcal{P}_k^{3\mathrm{D}} = \mathcal{P}_k - \mathcal{P}_k^{2\mathrm{D}} = -2\overline{u'w'}S_{13} - 2\overline{v'w'}S_{23}$. This decomposition provides evidence for the claim made above regarding the importance of the spanwise shear as the chordwise flow approaches separation, in that $\mathcal{P}_k^{2\mathrm{D}} \to 0$ and $\mathcal{P}_k^{3\mathrm{D}}$, while weakening, remains finite. Note that the maximum $\mathcal{P}_k^{3\mathrm{D}}$ is located near the wall for all ξ. The 'u_τ-component' inner scaling used for the maximum chordwise and spanwise production in figure 5*b* reveals the conversion from the collateral to the APG-layer state for Case C35, in that $\mathcal{P}_k/u_\tau^4$ for Case C0 and $\mathcal{P}_k^{2\mathrm{D}}/u_{\tau_x}^4$ and $\mathcal{P}_k^{3\mathrm{D}}/u_{\tau_z}^4$ all agree in the pure ZPG region, before they diverge. (Recall that for a collateral/ZPG layer, the chordwise or spanwise component shear stress and corresponding mean wall-normal velocity gradient, and thus the wall stress, are all proportional to the sine or cosine of the sweep angle.) That $\mathcal{P}_k/u_\tau^4$ and $\mathcal{P}_k^{2\mathrm{D}}/u_{\tau_x}^4$ exhibit similar behavior – both in terms of the values and locations of their maxima – across the ZPG, APG, and early FPG regions is consistent with the validity of the Independence Principle in the low-C_{f_x} zone bridging the bubble (which, based on figure 6*b* of CRS19, corresponds to about $5.5 \leq \xi/Y \leq 11.5$).

Another similarity between the swept and unswept flows is found in the scalar 'productive stress' field, $\tau_{\mathrm{prod}} \equiv \rho\mathcal{P}_k/\sqrt{2S_{ij}S_{ij}}$. This quantity represents the energy transfer between the turbulence and the mean flow, and is thus important in both

theoretical and modeling contexts. The trajectory of the magnitude and location of its maximum is illustrated in figure 5*c*. The Case C0 result is a distillation of the 2D, x-y data shown in figure 13*f* of CRS18. The shapes of the chordwise variations of the Case C0 and C35 magnitudes are quite similar, with the difference in their peaks near $\xi/Y = 6.5$ again in line with the differences of their $u_\tau(\xi_0)/\widetilde{\delta}_{995_x}(\xi_0)$ ratios; the locations of the maxima agree surprisingly well, with the only meaningful discrepancy being the earlier return of the maximum, downstream of reattachment, from the outer to the inner layer for the swept flow, caused by the nonzero spanwise shear. The other coordinate-independent quantity shown in figure 5*c* (shaded/grey curves) is the norm of the trace-free part (deviator) of the Reynolds-stress tensor, $\tau_{\rm dev}/\rho = \sqrt{d_{ij}d_{ij}/2}$, where $d_{ij} = \overline{u_i'u_j'} - (2k/3)\delta_{ij}$. Because of the strong Reynolds-stress anisotropy, especially near the wall, over most of the flow the magnitude and location of its maximum are significantly different than those of the productive stress. The chordwise variation of the maximum $\tau_{\rm dev}$ for the swept and unswept cases do not reveal a profound dependency on the presence of sweep, except for the tendency for the near-wall maximum to again remain dominant deeper into the APG, and earlier into the FPG, for Case C35. The outer-layer locations of the maxima agree closely with those for the productive stress, for the swept and unswept flows.

The ratio of the productive stress to the TKE is also relatively indifferent to sweep, as can be seen in figure 5*d*. This ratio can be viewed as a measure of the efficiency of the energy and momentum transfer from the mean flow by the turbulence. Also included (shaded/grey curves) is the oft-used 'structure parameter' $a_1 = |\tau_{xz}|/\rho k$, with (to account for the boundary-layer skewing) the numerator now defined as the magnitude of the x-z shear stress, with $|\tau_{xz}/\rho|^2 = \overline{u'v'}^2 + \overline{v'w'}^2$. Although these ratios are equivalent for parallel/unidirectional shear flow, for spatially developing pressure-gradient layers they exhibit quantitatively different behavior, in that the maximum a_1 decreases under the influence of the APG here, while the actual transfer-efficiency ratio does the opposite. In CRS18, it was found that replacing the a_1 numerator by the Reynolds shear stress component aligned with the local mean streamline removes this qualitative discrepancy in the APG regions, but not all quantitative differences with the $\tau_{\rm prod}$-based ratio. As was stressed in CRS18, slight streamline divergence can have a surprisingly large impact on the measures developed, and the insight gleaned, from studies of parallel thin-shear layers.

In contrast to the TKE profiles, the transfer-efficiency ratio has one local, outer-layer, maximum at each chordwise location (cf. figure 13*h* of CRS18), whose value is only somewhat affected by sweep. There is a modest reduction in the APG region, perhaps due to the 'sideways-toppling-eddy' mechanism, proposed by Bradshaw & Pontikos [2] (see also Schwarz & Bradshaw [15] to reduce the energy transfer efficiency in the outer layer. But overall, we are left to conclude (with Coleman, Kim & Spalart [16], based on their strained-channel study) that the APG strain has a much more profound effect, for example in near-wall TKE reduction, than the skewing does on the boundary-layer turbulence.

5 Closing comments

The discussion above demonstrates the manner in which the Case C35 DNS data can be used, in this instance to ascertain the relative insignificance of the spanwise mean strain upon the turbulence structure in swept decelerating boundary layers. Other issues, involving basic questions such as the relevance of the Independence Principle and the behavior of lower-order statistics, are taken up in CRS19. The Case C35 database, including thicknesses, skin friction, and mean-velocity and Reynolds-stress fields, which is available from the NASA Turbulence Modeling Resource website, https://turbmodels.larc.nasa.gov, is offered as a benchmark for other DNS, LES and RANS studies, and to guide turbulence theory and RANS modeling.

References

1. Coleman, G. N., Rumsey, C. L. & Spalart, P. R. 2019 Numerical study of a turbulent separation bubble with sweep. *J. Fluid Mech.*, submitted March 2019 (referred to herein as CRS19).

2. Bradshaw, P. & Pontikos, N. S. 1985 Measurements in the turbulent boundary layer on an 'infinite' swept wing. *J. Fluid Mech.* **159**, 105–130.

3. Driver, D. M. & Johnson, J. P. 1990 Experimental study of a three-dimensional shear-driven turbulent boundary layer with streamwise adverse pressure gradient. *NASA Tech. Mem.* 102211.

4. Berg, B. van den, Elsenaar, A., Lindhout, J. P. F. & Wesseling, P. 1975 Measurements in an incompressible three-dimensional turbulent boundary layer, under infinite swept-wing conditions, and comparison with theory. *J. Fluid Mech.* **70**, 127–148.

5. Coleman, G. N., Rumsey, C. L. & Spalart, P. R. 2018 Numerical study of turbulent separation bubbles with varying pressure gradient and Reynolds number. *J. Fluid Mech.* **847**, 28–70 (referred to herein as CRS18).

6. Spalart, P. R., Moser, R. D. & Rogers, M. M. 1991 Spectral solvers for the Navier-Stokes equations with two periodic and one infinite direction. *J. Comp. Phys.* **96**, 297–324.

7. Spalart, P. R. & Coleman, G. N. 1997 Numerical study of a separation bubble with heat transfer. *Eur. J. Mech., B/Fluids* **16**, 169–189 (referred to herein as SC97).

8. Coleman, G. N., Ferziger, J. H. & Spalart, P. R. 1990 A numerical study of the stratified turbulent Ekman layer. *Dept. of Mech. Engng, Stanford University, Thermosciences Div. Rep. TF*-48.

9. Coles, D. E. 1962 The turbulent boundary layer in a compressible fluid. *Rand Rep.* R403-PR, ARC 24473: Appendix A: A manual of experimental practice for low-speed flow.

10. Spalart, P. R. & Watmuff, J. H. 1993 Experimental and numerical study of a turbulent boundary layer with pressure gradients. *J. Fluid Mech.* **249**, 337–371.

11. Spalart, P. R. 1988 Direct simulation of a turbulent boundary layer up to $R_\theta = 1410$. *J. Fluid Mech.* **187**, 61–98.

12. Schlatter, P. & Örlü, R. 2010 Assessment of direct numerical simulation data of turbulent boundary layers. *J. Fluid Mech.* **659**, 116-126.

13. Sillero, J. A., Jiménez, J. & Moser, R. D. 2013 One-point statistics for turbulent wall-bounded flows at Reynolds numbers up to $\delta^+ \approx 2000$. *Phys. Fluids* **25**, 105102.

14. Luchini, P. 2018 Structure and interpolation of the turbulent velocity profile in parallel flow. *Eur. J. Mech., B/Fluids* **71**, 15–34.

15. Schwarz, W. R. & Bradshaw, P. 1994 Turbulence structural changes for a three-dimensional turbulent boundary layer in a 30° bend. *J. Fluid Mech.* **272**, 183–209.

16. Coleman, G. N., Kim, J. & Spalart, P. R. 2000 A numerical study of strained three-dimensional wall-bounded turbulence. *J. Fluid Mech.* **416**, 75–116.

REPORT DOCUMENTATION PAGE

Form Approved
OMB No. 0704–0188

1. REPORT DATE *(DD-MM-YYYY)*	2. REPORT TYPE	3. DATES COVERED *(From - To)*
01-04-2019	Technical Memorandum	

4. TITLE AND SUBTITLE
Numerical Study of the Effect of Mean Three-Dimensionality on Turbulence in Adverse-Pressure-Gradient Boundary Layers

5a. CONTRACT NUMBER

5b. GRANT NUMBER

5c. PROGRAM ELEMENT NUMBER

6. AUTHOR(S)
G. N. Coleman, C. L. Rumsey, P. R. Spalart

5d. PROJECT NUMBER

5e. TASK NUMBER

5f. WORK UNIT NUMBER
109492.02.07.01.05

7. PERFORMING ORGANIZATION NAME(S) AND ADDRESS(ES)
NASA Langley Research Center
Hampton, Virginia 23681-2199

8. PERFORMING ORGANIZATION REPORT NUMBER
L–21014

9. SPONSORING/MONITORING AGENCY NAME(S) AND ADDRESS(ES)
National Aeronautics and Space Administration
Washington, DC 20546-0001

10. SPONSOR/MONITOR'S ACRONYM(S)
NASA

11. SPONSOR/MONITOR'S REPORT NUMBER(S)
NASA/TM–2019–220273

12. DISTRIBUTION/AVAILABILITY STATEMENT
Unclassified-Unlimited
Subject Category 02
Availability: NASA STI Program (757) 864-9658

13. SUPPLEMENTARY NOTES

14. ABSTRACT

Direct numerical simulation (DNS) is used to isolate the influence of sweep on a separating turbulent boundary layer. Attention here is limited to the behavior of the turbulence within the adverse-pressure-gradient (APG) region upstream of separation. Other regions and quantities are considered in Coleman, Rumsey & Spalart [1]. The mean three-dimensionality and outer-layer inviscid skewing have only a slight effect upon the structure of the turbulence (measured by the relationship of the components of the Reynolds-stress tensor and the efficiency of the turbulence energy transfer) compared with that of the adverse pressure gradient, which dominates both the skewed and unskewed layers.

15. SUBJECT TERMS

16. SECURITY CLASSIFICATION OF:			17. LIMITATION OF ABSTRACT	18. NUMBER OF PAGES	19a. NAME OF RESPONSIBLE PERSON
a. REPORT	b. ABSTRACT	c. THIS PAGE			STI Information Desk (help@sti.nasa.gov)
U	U	U	UU	18	19b. TELEPHONE NUMBER *(Include area code)* (757) 864-9658